



# Climate, weather, and north polar observations from the Mars Reconnaissance Orbiter Mars Color Imager

Michael C. Malin<sup>a</sup>, Wendy M. Calvin<sup>c</sup>, Bruce A. Cantor<sup>a</sup>, R. Todd Clancy<sup>d</sup>, Robert M. Haberle<sup>e</sup>, Philip B. James<sup>g,\*</sup>, Peter C. Thomas<sup>g</sup>, Michael J. Wolff<sup>d</sup>, James F. Bell III<sup>b</sup>, Steven W. Lee<sup>d,f</sup>

<sup>a</sup> Malin Space Science Systems, P.O. Box 910149, San Diego, CA 92191, USA

<sup>b</sup> Cornell University, Department of Astronomy, Ithaca, NY 14853, USA

<sup>c</sup> University of Nevada, Reno, Department of Geological Sciences, Reno, NV 89557, USA

<sup>d</sup> Space Science Institute, 4750 Walnut St., Suite 205, Boulder, CO 80301, USA

<sup>e</sup> NASA Ames Research Center, Moffett Field, CA 94035, USA

<sup>f</sup> Denver Museum of Nature and Science, 2001 Colorado Blvd., Denver, CO 80205, USA

<sup>g</sup> Cornell University, Center for Radiophysics and Space Research, Ithaca, NY 14853, USA

Received 31 August 2007

Available online 22 November 2007

## Abstract

The Mars Reconnaissance Orbiter observes Mars from a nearly circular, polar orbit. From this vantage point, the Mars Color Imager extends the ~5 Mars years record of Mars Global Surveyor global, visible-wavelength multi-color observations of meteorological events and adds measurements at three additional visible and two ultraviolet wavelengths. Observations of the global distribution of ozone (which anti-correlates with water vapor) and water ice and dust clouds allow tracking of atmospheric circulation. Regional and local observations emphasize smaller scale atmospheric dynamics, especially those related to dust lifting and subsequent motion. Polar observations detail variations related to the polar heat budget, including changes in polar frosts and ices, and storms generated at high thermal contrast boundaries.

© 2007 Elsevier Inc. All rights reserved.

**Keywords:** Mars, atmosphere; Mars, polar caps

## 1. Introduction

The Mars Color Imager (MARCI) on-board the Mars Reconnaissance Orbiter (MRO) provides global and regional imaging capabilities for climatological and meteorological studies (Malin et al., 2001). MARCI is a very wide angle (180° field-of-view, FOV) push-frame camera that includes 7 color bands (260, 320, 420, 550, 600, 650, 750 nm) designed primarily to monitor atmospheric and polar processes. MARCI data are typically acquired at a resolution of about 900 m/pixel at the nadir from 300 km altitude on pole-to-pole swaths on the sunlit side (~1500 local mean solar time—LMST—equator-crossing) of every orbit, providing views limb-to-limb across the entire

ground track. Adjacent orbits barely overlap at the equator, but substantial overlap occurs in the polar regions. MARCI began imaging Mars on a daily basis on 24 September 2006, prior to conjunction and the start of the Primary Science Phase. MARCI observations will extend continuous daily global observations of Mars made during the previous ~5 Mars years (9 Earth years) by the Mars Global Surveyor (MGS) Mars Orbiter Camera (MOC) Wide-Angle Camera (WA). However, the capabilities of MARCI exceed those of MOC WA in several respects: UV coverage, spectral resolution and spatial resolution of the daily maps. Here we report results from the first ~100 days of MRO measurements in five areas that illustrate these unique MARCI capabilities: ultraviolet observations, orographic clouds, polar transient baroclinic eddies, dust storms (including polar and tropical spiral storms), and polar albedo relations.

\* Corresponding author.

E-mail address: [pjames@cableone.net](mailto:pjames@cableone.net) (P.B. James).

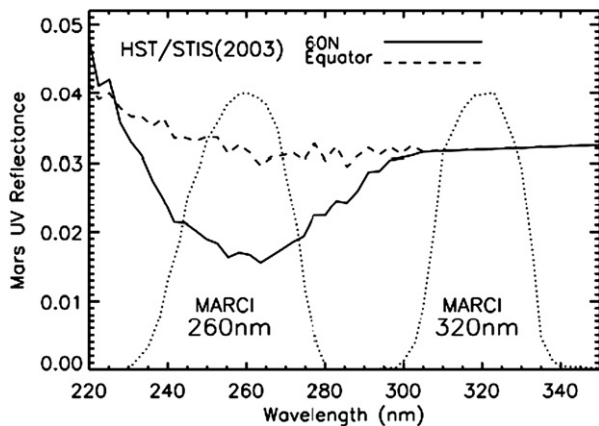


Fig. 1. MARCI UV bandpasses with respect to HST UV observations of Mars.

## 2. UV observations

### 2.1. Cloud distribution

MARCI has two middle ultraviolet (UV) channels at  $260 \pm 30$  and  $320 \pm 25$  nm. The spectral locations of these channels are designed to measure the Hartley band absorption of Mars atmospheric ozone, which reaches a maximum in the 260 nm channel and minimally contributes to the 320 nm channel. Fig. 1 shows the MARCI UV bandpasses in the context of two Mars ultraviolet spectra observed during the 2003 northern fall season ( $L_s = 182^\circ$ ) with the Hubble Space Telescope (HST), Space Telescope Imaging Spectrograph (STIS) for a low latitude, low column ozone region (dashed line) and a high latitude ( $60^\circ$  N), high ozone column region (solid line) (Clancy et al., 1999). For this comparison, the STIS spectra have been extrapolated with a constant value at wavelengths longer than 320 nm, where their reflectance values are normalized. Mars reflectance over these UV wavelengths is affected by the low albedo surface (of order 0.01, except for ice covered surface regions), Rayleigh scattering from the molecular atmosphere, dust aerosol scattering/absorption, ice cloud scattering, and Hartley band ozone absorption. Apart from seasonal polar ice coverage, the UV surface reflectance of Mars exhibits modest spatial and wavelength variations as compared to visible and near infrared wavelengths (James et al., 1994; Perrier et al., 2006). MARCI UV images provide the first clear evidence of distinct spatial variations in Mars UV reflectance. Variations in Rayleigh scattering opacity are quantitatively defined by the known spatial and seasonal variations in surface pressure associated with topography and  $\text{CO}_2$  seasonal ice formation, respectively. Mars atmospheric dust presents low contrast at UV wavelengths owing to competing absorption and scattering contributions (see following section). Generally speaking, Mars 320 nm reflectance varies primarily as a consequence of spatial and temporal variations in atmospheric cloud columns. The 260 nm reflectance is additionally affected by spatial and temporal variations in atmospheric ozone columns.

The capacity of MARCI 320 nm images to map water-ice cloud opacities in the martian atmosphere is demonstrated in Fig. 2 (left). Central portions (emission angles of  $0 \pm 18^\circ$ ) of 65

individual orbit pole-to-pole strips have been compiled to construct a simple cylindrical map of Mars at 320 nm reflectance ( $I/F$ ), which varies from low  $I/F$  values of 0.01 at southern mid-latitudes to peak values of 0.10 associated with clouds over Olympus Mons and surface ice in the north polar region. The distinctive vertical boundaries between individual orbit swaths in this figure result from the discontinuous temporal sampling that characterizes such an image map constructed from 7 consecutive days (8–15 November 2006;  $L_s = 132.2^\circ$ – $135.9^\circ$ ) of 13 orbits/day. Owing to the asynchronous orbital period, adjacent image strips in this map projection are separated by up to several days in time such that the time variable cloud distribution appears discontinuous in longitude. Operationally, MARCI UV cloud and ozone maps are constructed from larger FOV portions of the MARCI images and assembled into daily global maps with occasional gaps in longitudinal coverage resulting from orbital altitude variations and off-nadir spacecraft pointing. Fig. 2 (left) demonstrates the global capability of the MARCI 320 nm channel to detect and characterize the distribution of clouds. The aphelion cloud belt is readily apparent as a broad longitudinal band of ice clouds centered at  $15^\circ$  N over the ascending branch of the late northern summer Hadley circulation (Clancy et al., 1996). Additional cloud structure is associated with elevated topographic regions (e.g., Tharsis volcanos), the Hellas basin, and winter southern high latitudes. UV reflectance over the north polar region is dominated by high surface ice albedos.

The MARCI UV cloud observations not only provide an improved Mars cloud climatology, they also provide important constraints for GCMs that simulate the martian water cycle. Clouds play a significant role in the exchange of water between hemispheres (Montmessin et al., 2004). The trapping and confinement effect of the aphelion cloud belt, for example, can determine the magnitude of net meridional transport (Clancy et al., 1996). Models that reproduce the observed distribution of water, both in vapor and cloud phases, will provide confidence in the conclusions drawn from them regarding the distribution of surface sources and sinks (other than the north residual cap).

We interpret the cloud patterns in Fig. 2 (left) using the latest version of the NASA Ames Mars GCM, which uses a moment order cloud microphysics scheme and assumes that the north residual cap is the only source of atmospheric water vapor (Haberle et al., 2007). Fig. 2 (right) shows the afternoon cloud column-opacities predicted by the model averaged over the same period included in the figure. Overall, a qualitative comparison with the MARCI 320 nm data is quite good as the model reproduces the aphelion cloud belt and its major structural features, as well as the southern mid-latitude clouds and Hellas enhancement. The only significant discrepancy is the cloud ensemble north of Syrtis Major ( $60^\circ$  N,  $270^\circ$  W), which is not seen in the images.

According to the model, the aphelion cloud belt forms when water subliming from the north polar residual cap is transported southward into the rising branch of the Hadley cell where it cools and condenses. In the model this occurs around the 1 mb level. The actual clouds are further modified locally by slope flows along the flanks of the volcanoes giving rise to some of

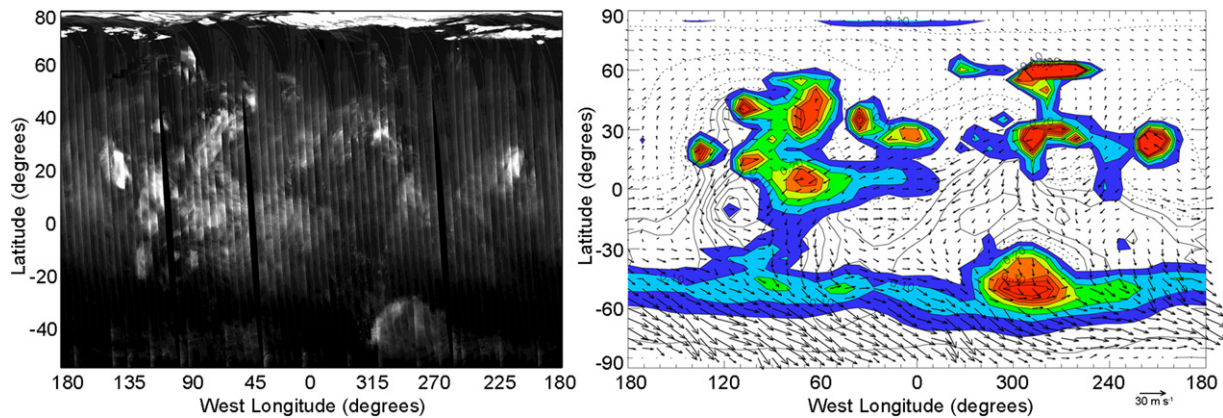


Fig. 2. (Left panel) UV reflectance from the MARCI 320 nm UV channel. Bright regions denote water-ice clouds. Global maps are constructed from 7 sols of observations (65 strips) over  $L_s = 132.2^\circ$ – $135.9^\circ$ . Individual orbit pole-to-pole strips have been compiled to construct a simple cylindrical map of Mars at 320 nm reflectance ( $I/F$ ) (7), which varies from low  $I/F$  values of 0.01 at southern mid-latitudes to peak values of 0.10, associated with clouds over Olympus Mons and surface ice in the north polar region. (Right panel) Time-averaged (10 sols) 1500 LMST 12- $\mu$ m column water-ice cloud opacities as simulated by the Ames Mars GCM for early northern summer,  $L_s = 127.9^\circ$ – $132.4^\circ$ . Color contour intervals are 0.1. Black contours (solid and dashed) are MOLA topography smoothed to the resolution of the GCM ( $5^\circ$  of latitude,  $9^\circ$  of longitude). Arrows represent time mean winds at 1.0 mbar level.

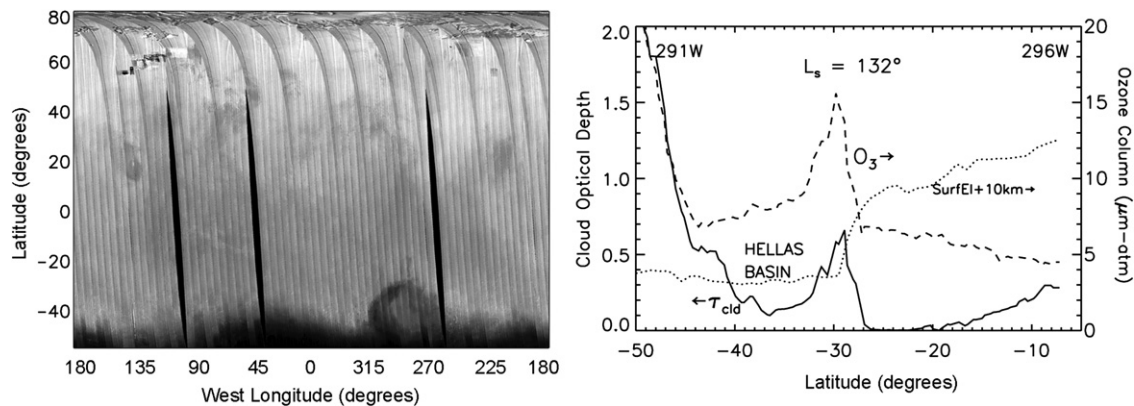


Fig. 3. (Left panel) UV image ratio (260–320 nm), corresponding to the 320 nm image map of Fig. 1. Dark regions indicate elevated atmospheric ozone columns. (Right panel) Radiative transfer derivations of 320 nm cloud optical depth (solid line) and ozone column (dashed line, in  $\mu\text{m-atm}$ ) for a latitudinal cross section through the Hellas Basin as observed in the left panel. MOLA surface elevations corresponding to the retrieved ozone, cloud cross-sections are presented by the dotted line (right scale minus 10 km = elevation).

the detailed structure in Fig. 2 (left); simulation of these details of the cloud formation requires a mesoscale model (Rafkin et al., 2002). The north cap also supplies water for the south mid-latitude clouds. In this case, however, it is the residual water vapor that has traversed the aphelion cloud belt, into the descending branch of the Hadley circulation, and has been transported further southward where temperatures are so cold that it eventually condenses. Consequently, these clouds form below the 1 mb level and extend to the surface. The enhanced cloudiness in Hellas may be related to the dynamical structure of the strong low-level cyclonic vortex its topography generates (not shown) and subsequent time-mean rising motion within the basin, and sinking motion along its flanks.

## 2.2. Ozone

The ability of MARCI 260 and 320 nm image ratios to map ozone columns in the martian atmosphere is demonstrated in Fig. 3 (left). This map-projected ratio image presents the two primary features of 260 to 320 nm reflectance ratios: 260 nm

reflectance decreases associated with ozone absorption, most apparent at high southern winter latitudes and within the Hellas basin; and 260 nm reflectance decreases owing to reduced Rayleigh scattering over low surface pressure, high altitude regions, most apparent over Tharsis and Elysium Mons. The discontinuous temporal coverage in this UV ratio mosaic imprints temporal variations onto longitudinal variations of low UV ratios, high ozone columns around the southern winter high latitude margin. Nevertheless, the larger longitudinal structures of ozone maxima associated with the Argyre and, most strikingly, Hellas Basins, are quite real. These features persist over  $L_s = 130^\circ$ – $145^\circ$ , although with substantial day-to-day variability in detailed spatial structure. The asymmetric appearance of the Hellas Basin in Fig. 3 (left) results from substantial daily variations associated with spatially variable cloud and ozone column variations.

The presence of ozone column increases over Hellas and Argyre Basins during comparable  $L_s$  periods of 45 and 120 in 2004 were observed with the SPICAM (Perrier et al., 2006) ul-



traviolet spectrometer. This phenomenon appears in ozone photochemical simulations with the Laboratoire de Meteorologie Dynamique (LMD) Mars General Circulation Model (GCM) (Montmessin et al., 2004), but not with sufficient spatial resolution to investigate the surprisingly asymmetric distributions in clouds and ozone columns visible in Fig. 3 (left) (Franck Lefevre, 2007, personal communication). The SPICAM point spectrometer observations are not designed to retrieve two-dimensional spatial distributions or obtain frequent temporal coverage.

Ozone and cloud optical depth column retrievals from MARCI UV imaging are well supported by the predominant and separable contributions of cloud scattering and ozone absorption. In Fig. 3 (right), we present radiative transfer derivations of 320 nm cloud optical depth (solid line) and ozone column (dashed line, in  $\mu\text{m-atm}$ ) for a latitudinal cross-section through the Hellas Basin as observed in Fig. 3 (left). The discrete ordinate multiple scattering code developed for general use by Stamnes et al. (1988) has been adapted to Mars atmospheric application for both aerosol (Clancy and Lee, 1991; Wolff et al., 1999; Clancy et al., 2003) and ozone (James et al., 1994; Clancy et al., 1995, 1999) retrievals, and is employed here. In the current model configuration, developed by Wolff et al. (2002), we specify spatial variation in the Rayleigh scattering column associated with topography (dotted line in Fig. 3 (right)), using the MOLA topographic data base (Smith et al., 2001); vertical profiles of dust, cloud, and ozone optical depth from the surface to 50 km altitude with 5 km intervals; Henyey–Greenstein single scattering phase functions for dust aerosols ( $g = 0.86$ ,  $w = 0.6$ ) and ice clouds ( $g = 0.83$ ,  $w = 1.0$ ), and a wavelength-independent Lambert albedo of 0.008–0.015 for the surface reflectance. A dust optical depth of 0.3 is specified with constant vertical mixing ratio, as this parameter is not well constrained by the data and is not a major contributor to retrieval uncertainties. The radiative transfer simulations of MARCI UV 260 and 320 nm calibrated  $I/F$  values are five-point wavelength averages, employing MARCI spectral response and solar flux spectral weights.

The retrieved peak ozone column values of 15  $\mu\text{m-atm}$  over Hellas Basin are consistent with SPICAM observations and LMD GCM model values at the southern margin of Hellas Basin at  $L_s = 120$ . The sharp decrease in the MARCI ozone columns over 32°–40° S, which was not observed by SPICAM owing to solar illumination constraints, indicates that the ozone column increase is not simply related to the increased surface pressure within the Hellas Basin. Southward of 38°–43° S cloud and ozone columns increase again, but there is a distinct 4°–5° latitudinal offset in the onset of these increases for ozone versus cloud columns. The striking correlation of cloud opacity and ozone column increases at the northern boundary of Hellas basin suggests important dynamical influences, as do the temporal variations of ozone and cloud opacity maxima associated with the Hellas and Argyre Basins.

The largest uncertainties in cloud optical depth retrievals from MARCI UV imaging relate to the adopted UV single scattering phase function of Mars water-ice clouds. The primary uncertainties affecting ozone column retrievals from MARCI

UV imaging are the relative radiometric calibration between the two UV channels, and the vertical distribution of ozone relative to cloud-, Rayleigh-, and surface-scattering. We have specified aphelion conditions for ozone and ice cloud vertical profiles in which clouds extend above 20 km altitudes and increased ozone densities above 20 km altitudes resulting from the low aphelion hygropause altitude (Clancy and Nair, 1996; Lefèvre et al., 2004). Currently, MARCI ozone and cloud column retrievals are most appropriate to mapping spatial and temporal distributions of Mars cloud and ozone columns with high precision (10–20%) but limited accuracy (30–50%).

### 2.3. Ultraviolet scattering properties of aerosols

The ultraviolet scattering properties of martian aerosols have not been particularly well constrained by earlier studies, largely because of limitations inherent in previous datasets. The Mariner 9 Ultraviolet Spectrometer (UVS) and the Mars Express SPICAM were designed as “spot” pointing instruments, and thus, their datasets do not provide the range of scattering geometry and spatial coverage needed. The Hubble Space Telescope (HST) UV spectrometers and imagers suffer from similar limitations in scattering geometry, with the addition of very limited temporal coverage. As a result, the combination of cross-track geometry (i.e., large range in scattering angle), daily global coverage, and multi-wavelength imaging offered by MARCI provides a unique opportunity for the characterization of UV aerosol properties, and more generally, for the microphysical properties of such particles. Although the current state of MARCI UV calibration is immature, initial results demonstrate this capability.

The occurrence of a large local dust storm in late December 2006 in Terra Cimmeria (southwest of Gusev crater) provides an excellent analysis opportunity to examine dust aerosol properties. Choosing an orbit from 29 December, which centers on this event, as well as one from 12 December for the same region that captures the atmospheric state before the storm and allows an estimate of the surface reflectance values, we performed a radiative transfer retrieval on both in-track and cross-track data strips using the 260, 320, and 425 nm images. Under the assumption of a wavelength-independent extinction cross-section, a Henyey–Greenstein scattering phase function, and a Lambert surface reflectance, the simultaneous fitting data in all three bandpasses produces single scattering albedo ( $\omega$ ) values of 0.51, 0.57, and 0.69 and asymmetry parameter ( $g$ ) values of 0.90, 0.87, and 0.70 (in order of increasing wavelength). The retrieved range of optical depths span from 0.4 (outside the storm) to 1.8–2.0 in the densest parts of the storm (as sampled). The Lambert albedo values estimated from the 12 December data are 0.01, 0.015, and 0.035–0.045 for the three bands, respectively. Finally, we estimated an ozone column that varies linearly from  $\sim 5 \mu\text{m-atm}$  at 10° S to  $\sim 9 \mu\text{m-atm}$  at 45° S.

Comparison to recent results using HST (Goguen et al., 2003) ( $\omega$ ,  $g = 0.64$ , 0.84 for 220–305 nm) and SPICAM (Mateshvilu et al., 2006) ( $\omega$ ,  $g = 0.60 \pm 0.04$ , 0,  $0.88 \pm 0.03$  at 213 nm and  $0.64 \pm 0.04$ ,  $0.86 \pm 0.03$  at 300 nm) reveals that although our asymmetry parameters are within estimated uncer-

tainties of  $\sim 0.03$ , our single scattering albedo values are somewhat darker even allowing for uncertainties in  $\varpi$  of  $\sim 0.03$ – $0.04$  (for 320 nm, larger for 260 nm). Although estimation of our retrieval uncertainties is complicated by the current state of the UV calibration, particularly at 260 nm, one would need to employ a larger asymmetry parameter in order to increase  $\varpi$ . The use of a Henyey–Greenstein function is a common, numerical convenience, not one based upon any realistic expectation for particles with the sizes of the canonical martian aerosols as viewed at optical wavelengths. The problem is exacerbated when attempting to compare results from data with different phase angle ranges: the SPICAM data are a series of in-track spot pointings and the HST data are limited by orbital relations to be within a narrow phase angle range whose values cannot exceed  $\sim 43^\circ$ . In other words, it is difficult to directly compare the results of the MARCI analysis which contains data with a phase angle range of  $\sim 40^\circ$  to  $125^\circ$  to the other two sets of values.

### 3. Visible cloud observations

#### 3.1. Orographic clouds

Simultaneous observations by MARCI and the MGS MOC Wide Angle Camera during the initial weeks of the MRO mission provided a unique opportunity to observe the semi-diurnal afternoon behavior of the orographic clouds over Olympus Mons during northern summer. Fig. 4 shows significant brightening of the Olympus Mons orographic clouds over just a 39-minute period, with peak ice-opacities increasing from 0.7 to 1.4. The clouds form as the air mass near the volcano is forced upwards, cooling as it rises until reaching its saturation point when ice clouds are formed. The circulation associated with the formation of clouds is due to a combination of thermally induced upslope flow and the rising branch of a mountain induced gravity wave (Michaels et al., 2006). The increased cloud-ice opacity indicates increased moisture convergence and uplift in the latter half of the afternoon. These observations are consistent with Viking observations of diurnal variations (Hunt et al., 1980); models (Wilson et al., 2006) suggest that these clouds

continue to grow during the nighttime. [Time-of-day differences in cloud opacities were previously observed with MOC, but those changes were noted between observations taken on consecutive sols (Benson et al., 2003).] The locations of the orographic clouds, which form on the windward side of the volcano, also indicate the direction of the general atmospheric circulation, which is from the WNW at this time of day and season.

#### 3.2. Baroclinic waves

MARCI observed the northern extratropical annular shaped water-ice cloud previously seen during the past five Mars years (Cantor et al., 2002). This year the phenomena occurred each day between  $L_s = 115.2^\circ$  and  $133.9^\circ$ . Initially, images showed the cloud forming in the early morning hours around 0300 local solar time (LST), but dissipating into convective cloud cells (5–15 km across) by 1500 LST. This diurnal cycle of relative growth and decay continued with the decay occurring later in each sol as the season progressed. By  $L_s = 121.3^\circ$ , the annular cloud structure was still noticeable at 1500 LST, though in the process of dissipating. The last late-afternoon view occurred on  $L_s = 133.9^\circ$ , after which the annular cloud did not fully reform again. This behavior might be the result of the seasonal weakening of the baroclinic eddy associated with the cloud's formation. The areal extent of such an eddy is consistent with northern summer mesoscale circulation model results (Tyler and Barnes, 2005).

In the latter-half of northern summer,  $L_s \sim 157.3^\circ$ , smaller transient baroclinic eddies were observed along the same longitude range as the annular water-ice cloud, at  $70.8^\circ$  N (Fig. 5). This is the first time such eddies have been observed in the martian atmosphere, although waves did return to the VL-2 pressure data in late summer (Hess et al., 1980). These eddies are similar to terrestrial polar baroclinic eddies, forming along the boundary of the polar jet stream, where lower pressure cold polar air meets the higher-pressure warmer extratropical circulation. These transient eddies lasted for only about 12 h, less than the terrestrial analogs, probably because of the shorter radiative time constant on Mars. Cloud streets, which are indicators of

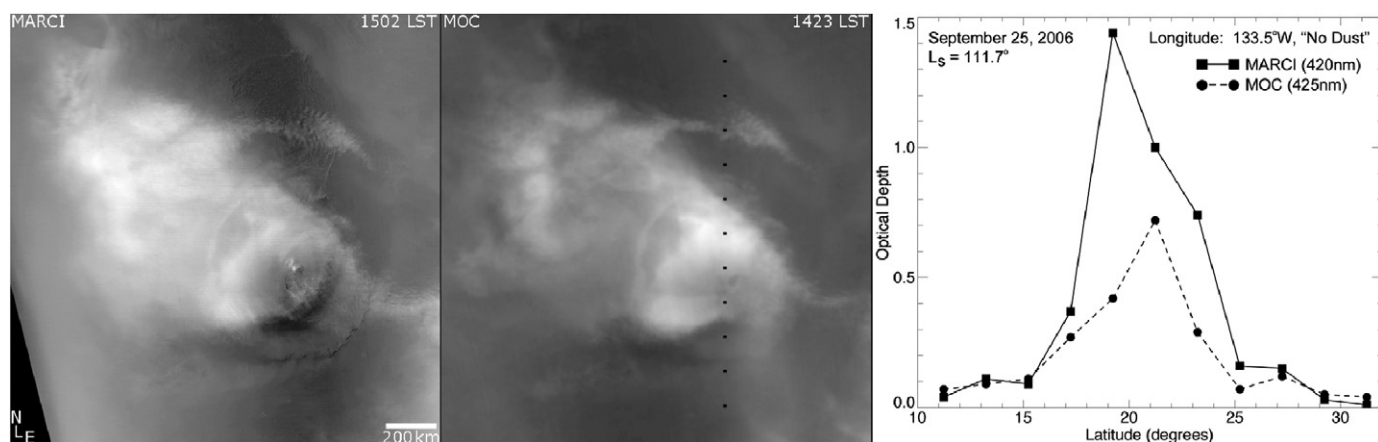


Fig. 4. Orographic clouds observed over Olympus Mons, (left) MRO-MARCI and (center) MGS-MOC during northern summer; (right) cloud opacities derived from a discrete ordinate multiple scattering radiative transfer (DISORT) code, using a surface Lambert albedo of 0.05.

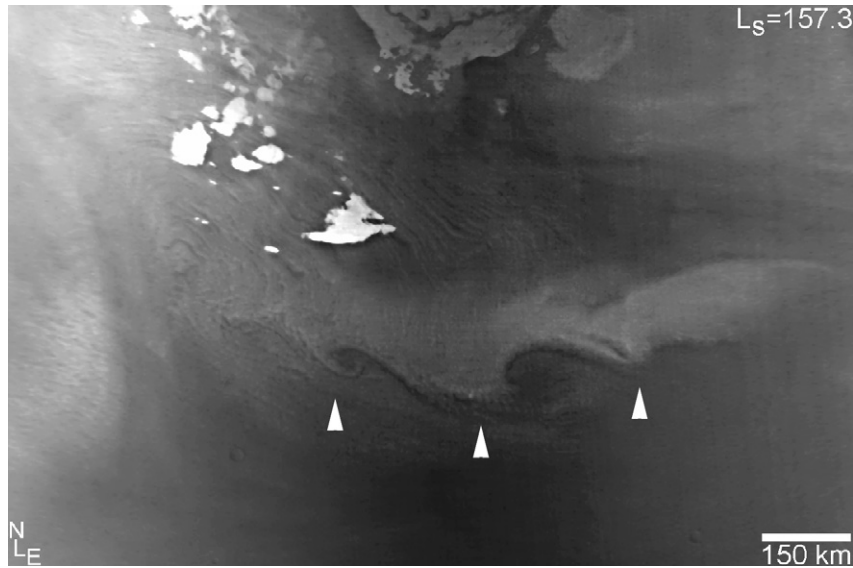


Fig. 5. North polar transient baroclinic eddies (arrows) observed in the MARCI blue (400 nm) bandpass. Image is a polar stereographic projection from  $65^{\circ}$ – $80^{\circ}$  N,  $56^{\circ}$ – $143^{\circ}$  W at a resolution of 1 km/pixel.

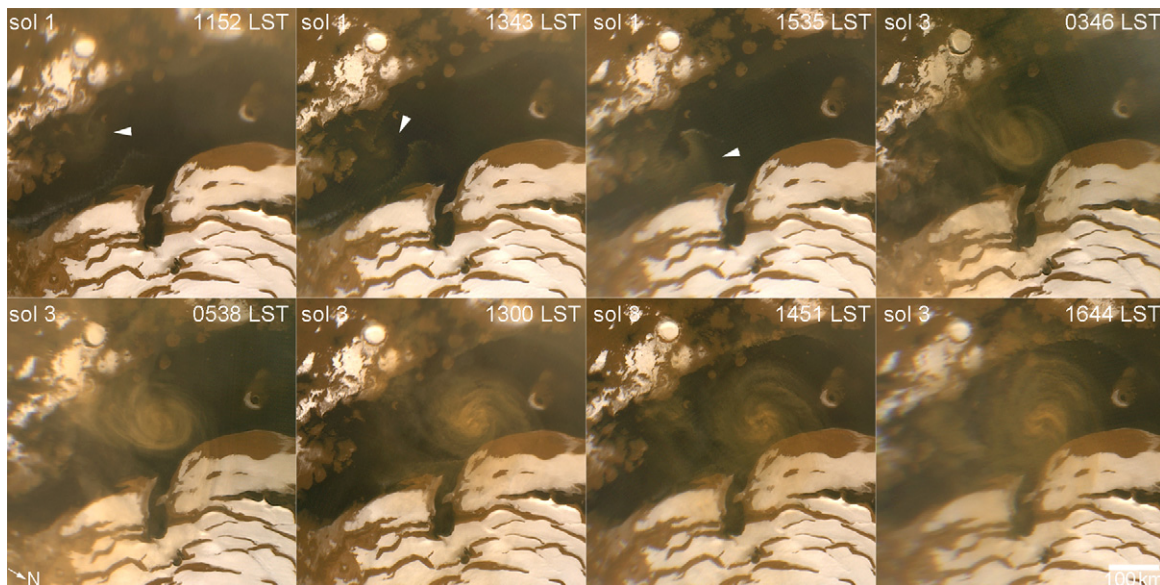


Fig. 6. Evolution of a spiral dust storm in Olympia Planitia over several sols. Images have been polar stereographically projected, centered at  $81.7^{\circ}$  N,  $143.0^{\circ}$  W, with a resolution of 1 km/pixel. Arrows in sol 1 images indicate the incipient storm.

vigorous circulation, extended over the north polar dune field, from the WNW.

### 3.3. Dust storms

On Earth, polar lows are characterized as short-lived ( $<36$  h) sub-synoptic (100–500 km) systems that are fundamentally baroclinic and/or convective in nature (e.g., Rasmussen and Turner, 2003). Spiral cloud patterns are a prominent feature of such systems and they often have a clear central eye suggesting they are warm core vortices analogous to tropical cyclones. Terrestrial examples generally develop rapidly when cold polar air moves over warm ocean waters, and then dissipate rapidly after landfall. Martian polar lows are similar. They have spi-

ral clouds and occasionally have clear central eyes (Fig. 6). The fact that they amplify in a low-albedo longitudinal corridor from  $120^{\circ}$ – $250^{\circ}$  W between  $79^{\circ}$ – $83^{\circ}$  N is consistent with receiving strong convective input from a warm surface. They rapidly dissipate when moving out of this corridor and over cooler terrains. This behavior has been captured in mesoscale model simulations of the atmosphere over the north polar residual cap (Tyler and Barnes, 2005). However, unlike their terrestrial counterparts, latent heat release is unlikely to play a central role in the dynamics of martian polar lows. Rather, dust lifting and heating may be more important (Hunt and James, 1979; Gierasch et al., 1979). The martian north polar spiral storms were observed to occur during a short seasonal window spanning  $L_s = 115^{\circ}$ – $122^{\circ}$ . The storms appeared to be initiated



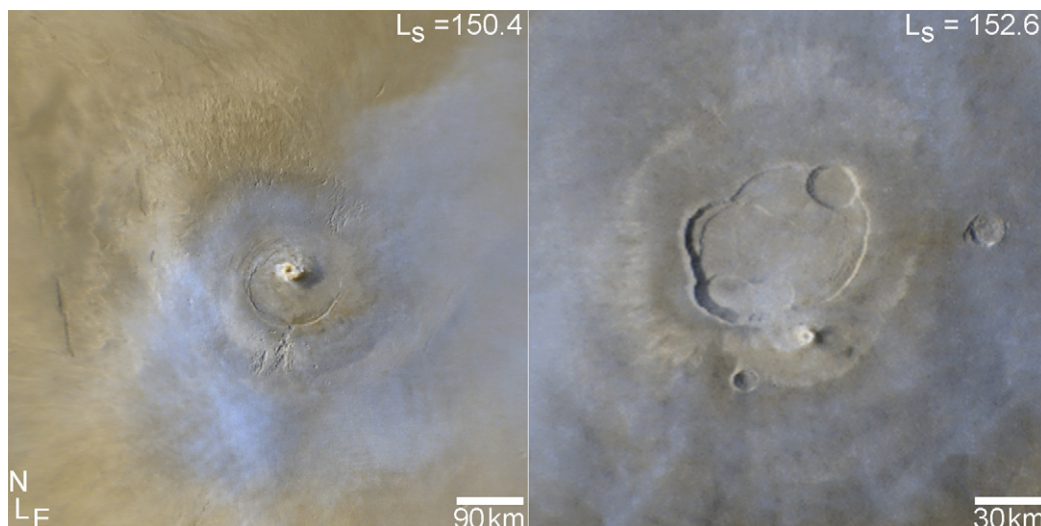


Fig. 7. Spiral dust storms over (left) Arsia Mons caldera and (right) near the caldera rim of Olympus Mons. Images are simple cylindrical map projections at 1 km/pixel.

along the boundary of the Olympia dune field and the polar-ice outliers to the south. The movement of these storms showed no systematic pattern.

Martian spiral storms have also been observed at tropical latitudes, in particular within the caldera of Arsia Mons, around the autumn equinox ( $L_s \sim 180^\circ \pm 7^\circ$ ) (Cantor et al., 2002; Rafkin et al., 2002). MARCI visible images showed that such storms can occur far earlier than previously recognized in MOC wide angle images (Fig. 7). MARCI images showed that such cyclonic dust and water-ice clouds are not limited to Arsia Mons. They were observed over all the Tharsis volcanoes and even at the highest elevation on the planet (the southern summit slope of Olympus Mons, at 20675 m above the mean martian geoid). The counter-clockwise rotation of these storms in the northern hemisphere and clockwise rotation in the southern hemisphere indicate that such storms are associated with low-pressure systems. Observations indicate that these weather systems may take up to 2–3 sols to fully spin-up to become a dust storm at which point they persist for less than an a single sol before dissipating. The lifetime of the majority of these systems is <1 sol.

The location of dust sources—areas where dust is actually lifted from the surface to create any given, observed dust storm has been one of the mysteries of Mars for decades. The higher spatial resolution of the daily mapping by MARCI relative to the MOC daily mapping resolution data, address this question. Select storms observed at southern mid-latitudes, near the receding seasonal south polar cap edge show streamers of dust extending west-to-east along the trailing edge of the storms near large craters and in the lee of small mountain ranges. These streamers are indicators of areas of active dust-lifting in the storms (Fig. 8). No shadows are observed associated with the streamers, indicating that they occur close to the surface, while the dust clouds that extend to the east from the streamers cast shadows indicating that they are much higher in the atmosphere. The faster winds at higher altitude move the dust clouds well to the east of the regions of active lifting. Such storms are similar

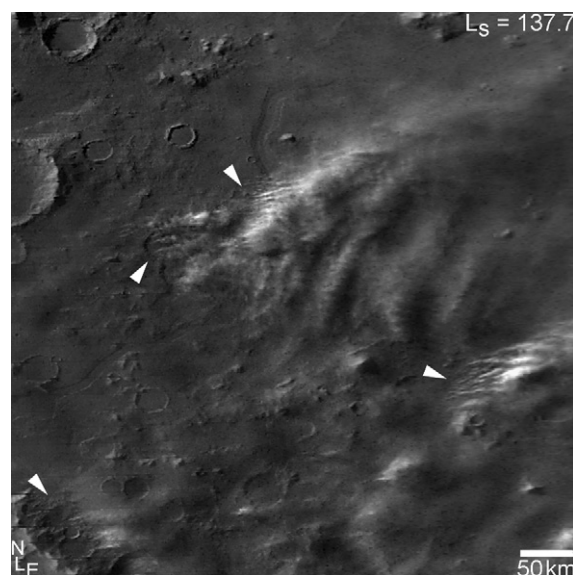


Fig. 8. Local dust storms in Promethei ( $38.4^\circ$  S,  $248^\circ$  W). Arrows indicate areas of active dust-lifting. MARCI (600 nm filter) image simple cylindrically projected at a resolution of  $\sim 1$  km/pixel.

to terrestrial squall-line weather systems where a low-pressure cold front passes over warmer air near the surface, forcing the warmer air to rise. This is likely the same situation on Mars. Such martian weather systems typically persist <3 sols before dissipating.

The fine surface dust lofted by local storms can easily reach the altitude at which water vapor is saturated in the cold thin martian atmosphere, providing the perfect nucleation sites for water ice. Water-ice clouds forming above very convective dust storms are common (Fig. 9).

### 3.4. Waves in Chasma Boreale

After the 1976–1980 Viking Orbiter missions, the martian north polar region was considered to be relatively dust free

compared the south polar region. This view was dispelled by nearly 5 Mars years of daily MGS MOC observations that showed dust activity in the two regions was comparable (Cantor et al., 2000, 2001). The eight times higher spatial resolution of MARCI data enables observation of key details of dust-raising activity in the polar regions. For example, in mid-December of 2006, prominent linear clouds, roughly parallel to the axis of Chasma Boreale, were observed for several hours (as viewed in MARCI images taken on successive 117 min orbits) (Fig. 10). These clouds are superposed on a generally hazy background and are characterized by a fairly sharp front on their eastern edges. Six distinct parallel clouds extend the length of Chasma Boreale. The two clouds closest to the axis of the chasma are especially bright, suggesting that they are composed of water ice as well as dust. During the period of observation the linear clouds moved towards the west, up the regional slope (Zuber et al., 1998), at speeds between 1.7 to 2.3 m/s (Fig. 10). The clouds dissipated where they encountered the steep sides of

Chasma Boreale suggesting they were in the lower atmosphere. Further up the slopes that lead to the pole the clouds are obscured by dust, reducing their apparent brightness almost 40% at blue wavelengths and about 25% at red wavelengths. The streaked appearance of the dust clouds to the west is characteristic of dust in motion. However, it is difficult to determine whether the dust is originating from exposed layers and troughs and thus moving down slope or from the Chasma Boreale and hence moving upslope.

These features superficially resemble the bore waves that were observed in the Tharsis region of Mars by Viking (Hunt et al., 1981; Kahn and Gierasch, 1982) that result from a katabatic front induced by strong, down slope flows induced by nighttime cooling on the slopes of the volcanoes (Sta Maria et al., 2006). However, the summit of the residual cap is illuminated all day, so the diurnal cycle is therefore relatively weak compared to Tharsis, and the model of Tyler and Barnes (2005) suggests katabatic flows in the 5–10 m/s range, lower than the 20 m/s range simulated for Tharsis. Thus it is unlikely that the phenomenon observed in the polar region is the same at the Tharsis bore wave. In addition, the observations indicate that the situation here is more complex. The movement of the polar waves is up-slope from east to west, rather than down slope as would be expected for a katabatic flow colliding with stationary atmosphere. These observations occurred at  $L_s = 149^\circ$ , the period when the summer atmospheric circulation pattern changes to that seen during the fall season (Tyler and Barnes, 2005) with a strong polar jet that supports the formation of baroclinic eddies; and such activity was observed in this sequence to the southeast of Chasma Boreale. In this case the situation might resemble the bore wave features observed through enhanced emissions in the Antarctica mesosphere by Nielsen et al. (2006). Further observations and modeling will be needed to understand the origin of these features discovered by MARCI.

#### 4. Perennial north polar cap

Dust storms over the polar caps can change the polar surface albedo and thereby the polar heat budget. Large regional storms are not required to change the surface albedo; a single local dust storm passing over the perennial cap can cause regional albedo changes that persisted for the duration of the period that the perennial cap was visible. For example, the storm shown in

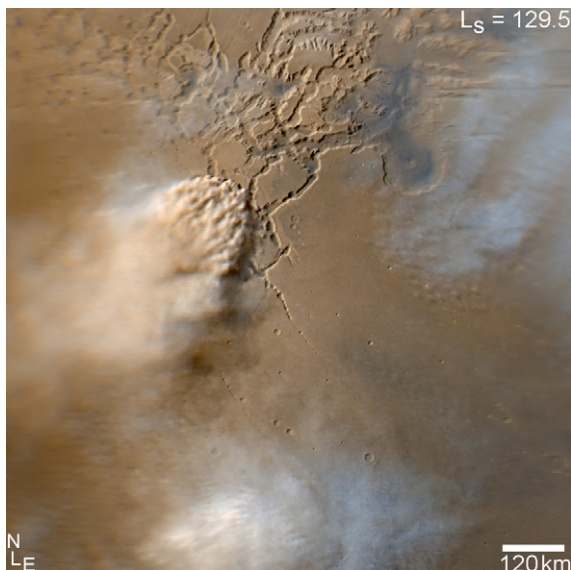


Fig. 9. Water-ice clouds (white or slightly blue) forming at the top of a local dust storm (yellow) in eastern Syria during southern winter. Although this particular storm was imaged only once, the motions of storms in this region is typically to the NE into Noctis Labyrinthus, consistent with MGCM simulations at this season. Image is a simple cylindrical map projection at a resolution of 1 km/pixel.

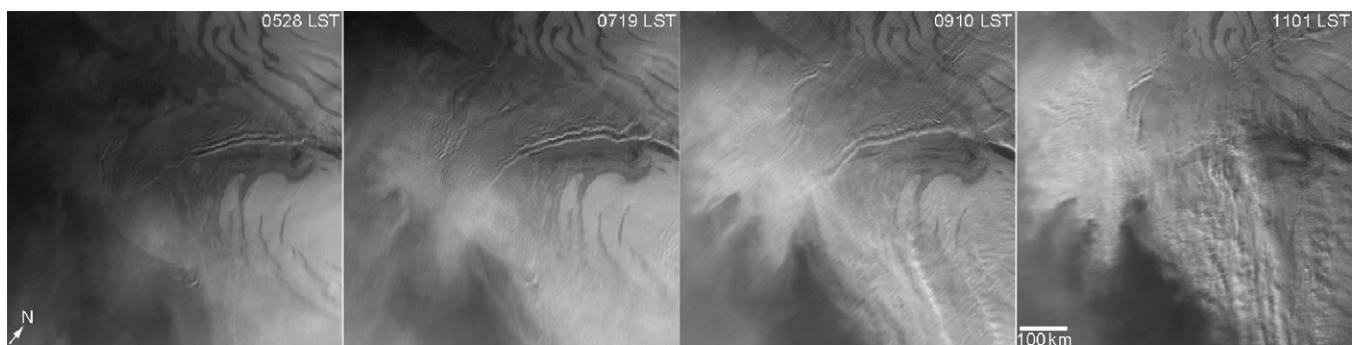


Fig. 10. Propagation of early morning north polar gravity wave clouds observed in Chasma Boreale on 12 December 2006. Images were obtained with the MARCI 600 nm filter and have been polar stereographically projected between  $80^\circ$ – $90^\circ$  N,  $0^\circ$ – $90^\circ$  W at a resolution  $\sim 1$  km/pixel.



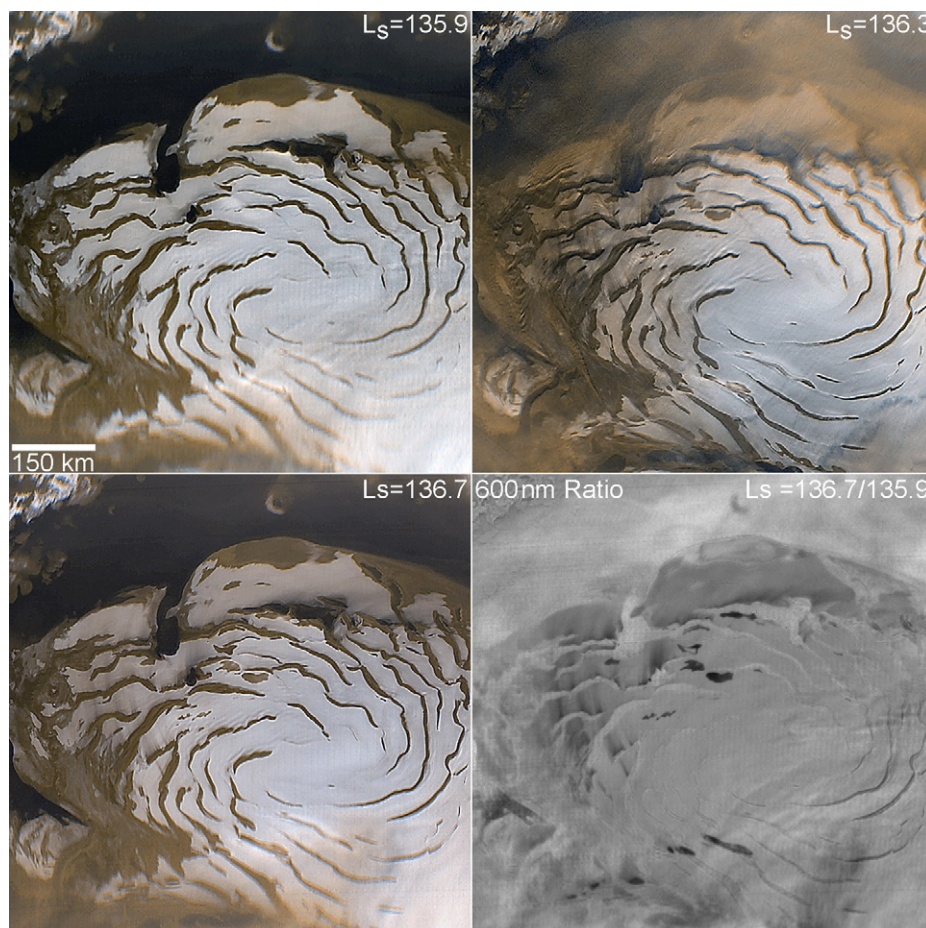


Fig. 11. Perennial north polar cap albedo changes resulting from local storm activity, observed during the summer season. Images are polar stereographic map-projections at a resolution of 1 km/pixel. The lower right shows the ratio from  $L_s = 135.9^\circ$  to  $136.7^\circ$ . Black arrows denote regions of large scale removal of surface ice (very dark patches) and deposition of dust (arcuate dark streaks on the left) after the small dust event seen the following sol at  $L_s = 136.3^\circ$ .

Fig. 11 was at first optically thin but became more opaque once it reached a source of dust the Olympia Planitia dune field. The storm moved from  $300^\circ$  W across the pole to the north and then moved to the south between  $100^\circ$ – $250^\circ$  W longitude. Dust streamers were seen faintly across the leading edge of the storm when it was over the cap. In this case, albedo changes were the result of the removal of surface frost through the effects of atmospheric dust on the energy balance, exposing the underlying bare terrain, rather than deposition of dust. Dust was also lifted from the frost-free exposed troughs, creating dust streaks emanating from the troughs in a west-southwest direction near the cap boundary.

The composition of the residual north polar cap of Mars is a mixture of dust in water ice (Kieffer et al., 1976). The physical state of the material in the cap is characterized mainly by the grain size (more correctly the photon mean free path) of the water ice and the amount of dust contamination. The wavelength dependence of the reflectivity of the ice is quite sensitive to these parameters and serves as a surrogate for determining their variation. The strengths of strong water-ice absorption bands at 1.5 and 2  $\mu\text{m}$ , depend sensitively on the grain size. The Mars Express Omega team measured a seasonal increase in the depth of water-ice absorption bands in the north polar ice deposits that

they attributed to sublimation of a layer of fine-grained material ( $\sim 100 \mu\text{m}$  grain size) that revealed a layer of larger grained ( $\sim 700$ – $800 \mu\text{m}$ ) material (Langevin et al., 2005).

The reflectance spectrum at visible wavelengths is most sensitive to the dust contamination of the ice deposits. The five relatively narrow MARCI visible filters provide good wavelength resolution in the visible part of the spectrum. MARCI images were selected on the basis of the longitude at which MRO crossed the equator ( $60 \pm 15^\circ$ W) in order to minimize variations in the orientation of the Sun relative to cap locations. These were projected into polar stereographic Lambert albedo maps by dividing each projected pixel by the cosine of the solar incidence angle. The albedo for an approximately 10 km region surrounding the geographic pole was determined from these maps; this point was chosen in order to minimize variations due to changes in the photometric angles. Fig. 12 shows the albedo as a function of wavelength for three images acquired at intervals of 20–30 days at values of  $L_s = 131^\circ$  (solid),  $144^\circ$  (dashed), and  $162^\circ$  (dot-dashed).

Langevin et al. (2005) found a grain size of about 1 mm at the same  $L_s$  as our first image in the previous year. For such a large grain size our relatively high blue albedo would imply very small dust admixtures  $\ll 0.01\%$  (G. Hansen, personal com-

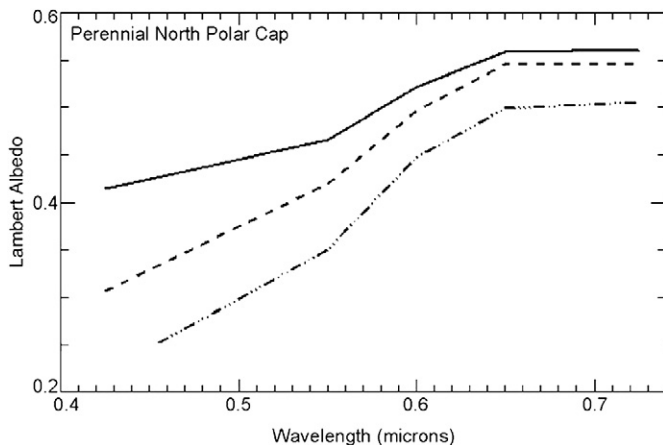


Fig. 12. Lambert albedos for region around the martian north pole as a function of wavelength. Solid curve is for  $L_s = 131^\circ$ ; dashed curve is for  $L_s = 144^\circ$ ; and the dot-dashed curve is for  $L_s = 162^\circ$ .

munication). On the other hand, long wavelength extrapolations of our measured albedos are very similar in absolute magnitude and variation to short wavelength extrapolations of those reported by Langevin et al. (2005). We suggest another possibility: that the seasonal variation that we observe is similar to theirs but delayed relative to their study region (at  $\sim 85^\circ$  N). This is consistent with the location and elevation of the summit of the north polar cap; we would expect that seasonal changes would occur last in that location, especially if recondensation of sublimed water vapor from outlying parts resurfaces the summit. If one adopts the grain size estimates reported by Langevin et al. (2005) for their earliest and latest observations, the amount of dust is estimated to be somewhat greater than 0.01% at both times (G. Hansen, personal communication). Whether or not our alternative interpretation is correct, the data support the conclusion that the residual ice at the summit of the cap contains very little dust contamination, unlike some other regions of the cap.

These changes in albedo could be effected by variations in atmospheric dust as well as by changes in surface properties. Atmospheric dust suppresses the albedo of the bright frost preferentially at the shorter wavelengths, so an increase in dust opacity in late summer could produce the trend in Fig. 12. It is not possible to rigorously correct for dust effects without independent measurements of the dust optical depth. In order to qualitatively monitor changes in opacity we monitored the albedo of a dark region near the edge of the cap for changes that would indicate changes in dust opacity. There was no change in the albedo of the dark region between the first two observations. After  $L_s = 150^\circ$ , the periphery of the residual north polar cap becomes noticeably dustier, and the albedo of the region increased somewhat for the  $L_s = 161^\circ$  case. However, localized dust incursions can normally be visually seen over the frosted surfaces, and there was no obvious incursion of dust over the center of the cap. Uniform background opacity could produce the same effect as the optical path length increases due to the decreasing solar elevation. Monitoring the central cap albedo from  $L_s = 150^\circ$ – $163^\circ$  indicated that there was no downward

trend in the albedo throughout the period despite an increase of almost a factor of 2 in incident path length.

Dependence of the phase function of the polar ice on photometric angles could also affect the albedo; the Lambertian phase function is only an approximation adopted because of ignorance of the true dependence. Only the incidence angle changed in our observations since the emission angle and azimuthal angle are fixed by our selection of orbits and location on the cap. However, the incidence angles are large and could produce a residual variation with season even after the cosine of the incidence angle is divided out.

## 5. Conclusions

MARCI has made the first global observations of the distribution and spatial structure (morphology) of water in the martian atmosphere in both condensate clouds and disseminated vapor (the latter by using the surrogacy of reduced ozone concentrations). During the season of observation, UV imaging showed the aphelion cloud belt and other cloud formations, and UV ratio images showed spatial and temporal variations in the concentration of ozone consistent with previous measurements made by spectrometers. Equally important, numerical general circulation models appear to faithfully recreate the patterns and distributions seen in MARCI data, improving the outlook for forecasting such attributes of martian meteorology.

Consecutive observations of the large martian volcanoes by the MGS MOC from its 1400 LMST orbit and MRO MARCI from its 1500 LMST orbit during the brief period both spacecraft were in operations (prior to the 2 November 2006 loss of MGS) revealed details of the rapid time and spatial evolution of orographic clouds on Mars. These clouds are important markers of atmospheric circulation, and resemble the orographic clouds associated with the interaction of terrestrial trade winds with tropical islands.

MARCI continued monitoring observations of the martian polar jet streams and baroclinic storms following the loss of MGS, insuring continuity of these important meteorological measurements. MARCI images also revealed previously unseen small, transient baroclinic eddies forming along the boundary of the north polar jet stream.

Spiral storms on Mars were first seen in Viking Orbiter images of the north polar region, and MGS MOC showed that these dust storms occurred at specific times each year and in specific locations, thus defining a martian “cyclone alley.” MARCI continued observations of these cyclonic storms at typically 3–4 times better spatial resolution. MOC first observed small cyclonic dust storms within the caldera of Arsia Mons, consistent with the chimney effect of rising atmosphere heated on the slopes of the volcano affected by Coriolis forces. These storms were also extremely limited in their time distribution. MARCI not only continued observing the Arsia Mons storms but discovered that other volcanoes, including Olympus Mons, displayed similar storms. The latter storms are noteworthy because they occur at the highest elevation on Mars.

For many decades the mechanisms for lifting dust from the martian surface and into dust storms has been debated. Two

alternatives were most often considered: convective lifting of dust, in the form of dust devils and other small convection centers, and as the result of surface horizontal wind stress. MGS MOC demonstrated that dust devils played no role in initiating dust storms (although they were important in creating the general dust pall over Mars), but recent MARCI results show dramatically that earlier Viking and MGS observation of isolated low altitude dust plumes actually feed into larger, local- and regional-scale dust clouds.

Following recent studies of time-dependent albedo variations within the north polar residual water-ice cap by the Mars Express OMEGA spectrometer, MARCI documented the ongoing albedo changes at both high spatial and temporal resolution, and confirmed that the residual cap retains very little dust contamination. From these observations we also note that the changes are not simultaneous everywhere in the polar cap, nor are the albedos. The progression of changes appears dependent on season, latitude and altitude.

## Acknowledgments

The authors express their deep appreciation to the many people who contributed substantively to the success of the MARCI investigation, including the MSSS engineering staff that designed, built, and tested the camera, the MSSS Operations team, and personnel at Lockheed Martin Space Systems and the Jet Propulsion Laboratory. This work was funded through JPL Contract 1275776.

## References

- Benson, J.L., Bonev, B.P., James, P.B., Shan, K.J., Cantor, B.A., Caplinger, M., 2003. The seasonal behavior of water-ice clouds in the Tharsis and Valles Marineris regions of Mars: Mars Orbiter Camera Observations. *Icarus* 165, 34–52.
- Cantor, B.A., James, P.B., Caplinger, M., Wolff, M.J., 2000. Martian dust storms: 1999–2000 MOC observations. *Bull. Am. Astron. Soc.* 32, 1094.
- Cantor, B., Malin, M.C., Edgett, K.S., 2001. Martian dust events: A global view by MOC. *Bull. Am. Astron. Soc.* 33, 1097.
- Cantor, B.A., Malin, M., Edgett, K.S., 2002. Multiyear Mars Orbiter Camera (MOC) observations of repeated martian weather phenomena during the northern summer season. *J. Geophys. Res.* 107 (E3), doi:10.1029/2001JE001588.
- Clancy, R.T., Lee, S.W., 1991. A new look at dust and clouds in the Mars atmosphere: Analysis of emission-phase-function sequences from global Viking IRTM observations. *Icarus* 93, 135–158.
- Clancy, R.T., Nair, H., 1996. Annual (perihelion–aphelion) cycles in the photochemical behavior of the global Mars atmosphere. *J. Geophys. Res.* 101, 12785–12790.
- Clancy, R.T., Lee, S.W., Gladstone, G.R., McMillan, W.W., Rousch, T., 1995. A new model for Mars atmospheric dust based upon analysis of ultraviolet through infrared observations from Mariner 9, Viking, and PHOBOS. *J. Geophys. Res.* 100, 5251–5273.
- Clancy, R.T., Grossman, A.W., Wolff, M.J., James, P.B., Rudy, D.J., Billawala, Y.N., Sandor, B.J., Lee, S.W., Muhleman, D.O., 1996. Water vapor saturation at low altitudes around Mars aphelion: A key to Mars climate? *Icarus* 122, 36–62.
- Clancy, R.T., Wolff, M.J., James, P.B., 1999. Minimal aerosol loading and global increases in atmospheric ozone during the 1996–97 martian northern spring season. *Icarus* 138, 49–63.
- Clancy, R.T., Wolff, M.J., Christensen, P.R., 2003. Mars aerosol studies with the MGS TES emission phase function observations: Optical depths, particle sizes, and ice cloud types versus latitude and solar longitude. *J. Geophys. Res.* 108 (E9), doi:10.1029/2003JE002058. CiteID 5098, 2–1.
- Gierasch, P.J., Thomas, P., French, R.G., Veverka, J., 1979. Spiral clouds on Mars: A new atmospheric phenomenon. *Geophys. Res. Lett.* 6, 405–408.
- Goguen, J.D., Clancy, R.T., Wolff, M.J., James, P.B., 2003. UV optical properties of aerosol dust from HST STIS spectra of Mars during the 2001 dust storm. *Bull. Am. Astron. Soc.* 35, 914.
- Haberle, R.M., Montmessin, F., Kahre, M., Schaeffer, J., 2007. Simulations of the martian water cycle with the Ames General Circulation Model: Comparison with Mars Express PFS/LW observations. In: European Geophysical Union Meeting, Vienna, Austria. Abstract No. EGU2007-A-04582.
- Hess, S.L., Ryan, J.A., Tillman, J.E., Henry, R.M., Leovy, C.B., 1980. The annual cycle of pressure on Mars measured by Viking Landers 1 and 2. *Geophys. Res. Lett.* 7, 197–200.
- Hunt, G.E., James, P.B., 1979. Martian extratropical cyclones. *Nature* 278, 531–532.
- Hunt, G.E., Pickersgill, A.O., James, P.B., Johnson, G., 1980. Some diurnal properties of clouds over the martian volcanoes. *Nature* 286, 362–364.
- Hunt, G.E., Pickersgill, A.O., James, P.B., Evans, N., 1981. Daily and seasonal Viking observations of martian bore wave systems. *Nature* 293, 630–633.
- James, P.B., Clancy, R.T., Lee, S.W., Martin, L., Kahn, R., Zurek, R., Singer, R., Smith, E., 1994. Monitoring Mars with Hubble Space Telescope: 1990–1991 observations. *Icarus* 109, 79–91.
- Kahn, K., Gierasch, P., 1982. Long cloud observations on Mars and implications for boundary layer characteristics over slopes. *J. Geophys. Res.* 87, 867–880.
- Kieffer, H.H., Martin, T.Z., Chase, S.C. Jr., Miner, E.D., Palluconi, F.D., 1976. Martian north pole summer temperatures: Dirty water ice. *Science* 194, 1341–1344.
- Langevin, Y., Poulet, F., Bibring, J.-P., Schmitt, B., Douté, S., Gondet, B., 2005. Summer evolution of the North Polar Cap of Mars as observed by OMEGA/Mars Express. *Science* 307, 1581–1584.
- Lefèvre, F., Lebonnois, S., Montmessin, F., Forget, F., 2004. Three-dimensional modeling of ozone on Mars. *J. Geophys. Res.* 109 (E07), doi:10.1029/2004JE002268.
- Malin, M.C., Calvin, W., Clancy, R.T., Haberle, R.M., James, P.B., Lee, S.W., Thomas, P.C., Caplinger, M.A., 2001. The Mars Color Imager (MARCI) on the Mars Climate Orbiter. *J. Geophys. Res.* 106 (E8), 17651–17672.
- Mateshvili, N., Fussen, D., Vanhellemont, F., Bingen, C., Dodion, J., Perrier, S., Bertaux, J.L., Dimarellis, E., Reberac, A., 2006. Detection of martian dust clouds by SPICAM UV nadir measurements during the October 2005 regional dust storm. In: 36th COSPAR Scientific Assembly, Beijing, China, 16–23 July 2006, p. 1593.
- Michaels, T., Colaprete, A., Rafkin, S.C.R., 2006. The significant vertical water transport by mountain-induced circulations on Mars. *Geophys. Res. Lett.* 33, doi:10.1029/GL026562. L16201.
- Montmessin, F., Forget, F., Rannou, P., Cabane, M., Haberle, R.M., 2004. Origin and role of water-ice clouds in the martian water cycle as inferred from a general circulation model. *J. Geophys. Res.* 109, doi:10.1029/2004JE002284. E10004.
- Nielsen, K., Taylor, M.J., Stockwell, R.G., Jarvis, M.J., 2006. An unusual mesospheric bore event observed at high latitudes over Antarctica. *Geophys. Res. Lett.* 33, L07803.
- Perrier, S., Bertaux, J.L., Lefèvre, F., Lebonnois, S., Korabiev, O., Fedorova, A., Montmessin, F., 2006. Global distribution of total ozone on Mars from SPICAM/MEX UV measurements. *J. Geophys. Res.* 111 (E9), doi:10.1029/2006JE002681.
- Rafkin, S.C.R., Sta. Maria, M.R.V., Michaels, T.I., 2002. Simulation of the atmospheric thermal circulation of a martian volcano using a mesoscale numerical model. *Nature* 419, 697–699.
- Rasmussen, E.A., Turner, J., 2003. Polar Lows, Mesoscale Weather Systems in the Polar Regions. Cambridge Univ. Press, Cambridge.
- Smith, D.E., and 23 colleagues, 2001. Mars Orbiter Laser Altimeter: Experiment summary after the first year of global mapping of Mars. *J. Geophys. Res.* 106, 23689–23722.
- Sta. Maria, M.R.V., Rafkin, S.C.R., Michaels, T.I., 2006. Numerical simulation of atmospheric bore waves on Mars. *Icarus* 185, 383–394.



- Stamnes, K., Tsay, S.C., Jayaweera, K., Wiscombe, W., 1988. Numerically stable algorithm for discrete-ordinate-method radiative transfer in multiple scattering and emitting layered media. *Appl. Opt.* 27, 2502–2509.
- Tyler, D., Barnes, J.R., 2005. A mesoscale model study of summertime atmospheric circulations in the North Polar Region of Mars. *J. Geophys. Res.* 110, doi:10.1029/2004JE002356. E06007.
- Wilson, R.J., Neumann, G., Smith, M.D., 2006. The diurnal variation and radiative influence of martian water-ice clouds. *Geophys. Res. Lett.* 34, doi:10.1029/2006GL027976. L02710.
- Wolff, M.J., James, P.B., Clancy, R.T., Lee, S.W., 1999. Water-ice clouds and diffuse dust: Hubble Space Telescope observations of the martian aphelion cloud belt prior to the Pathfinder mission: Seasonal and interannual variations. *J. Geophys. Res.* 104, 9027–9042.
- Wolff, M.J., Bell, J.F., Sohl-Dickstein, J., 2002. The single scattering albedo of martian atmospheric dust in the 290–500 nm region. In: AGU Fall Meeting 2002. Abstract #P72A-0494.
- Zuber, M.T., and 20 colleagues, 1998. Observations of the North Polar Region of Mars from the Mars Orbiter Laser Altimeter. *Science* 282, 2053–2060.